Journal of Multidisciplinary Engineering Science Studies (JMESS)
ISSN: 2458-925X
Vol. 12 Issue 2, February - 2026

Finite-Window Stochastic Geometry Modelling Of Campus Cellular Deployments For Coverage And Rate Analysis

[1]**Udekwe Charles Nnamdi**
Department of Information and Communication Engineering
Federal University of Technology Akure
Ondo State, Nigeria
cnudekwe@futa.edu.ng

[2]**Ponnle Akinlolu Adediran**
Department of Electrical and Electronics Engineering
Federal University of Technology Akure
Ondo State, Nigeria
aaponnle@futa.edu.ng

[3]**Folashade Mojisola Dahunsi**
Department of Computer Engineering
Federal University of Technology Akure
Ondo State, Nigeria
fmdahunsi@futa.edu.ng

[4]**Kazeem Bolade Adedeji**
Department of Electrical and Electronics Engineering
Federal University of Technology Akure
Ondo State, Nigeria
kbadedeji@futa.edu.ng

***Abstract*—Accurate spatial modelling of base-station deployments is essential for predicting coverage and rate performance in localized cellular networks. Infinite-plane models often neglect boundary effects and deployment irregularities typical of campus infrastructures. This study develops a finite-window stochastic-geometry framework for evaluating downlink coverage and rate within a bounded campus region. Measured base-station coordinates from the Federal University of Technology Akure (FUTA) were used to calibrate a homogeneous Poisson point process baseline, while a density-matched Hexgrid deployment served as a structured benchmark. Edge bias was mitigated through periodic wrap-around modelling. Performance was assessed under empirical FUTA, 3GPP Urban Macro, and power-law (α=4) pathloss models in both noise- and interference-limited regimes. Structured geometry improved coverage by approximately 12% at 0 dB under 3GPP, with gains reducing to 1–2% at 20 dB and about 3% under empirical calibration. Absolute rate coverage at 10 Mbps improved by roughly 11% under standardized propagation. While regular layouts provide upper-bound performance, stochastic modelling more accurately reflects observed campus deployment behaviour.**

Keywords—Stochastic-geometry, Point-process; style, finite-window, Coverage probability, Rate probability

I. INTRODUCTION

Accurate spatial modelling of base-station (BS) deployments is fundamental to understanding coverage and rate performance in cellular networks. Classical cellular analysis often assumes idealized hexagonal grid layouts [1][2]; however, real-world deployments rarely exhibit such regularity due to terrain constraints, zoning policies, infrastructure availability, and traffic heterogeneity. This mismatch between classical grid abstractions and real deployments motivated the widespread adoption of Stochastic Geometry (SG) as a mathematical framework for cellular-network analysis [1][2]. Within SG, the Homogeneous Poisson Point Process (HPPP) has emerged as the canonical baseline model. Its analytical tractability allows closed-form or semi-closed-form expressions for the coverage probability under Rayleigh fading and power-law pathloss assumptions [1]. These results have shaped modern understanding of interference-limited behavior, density invariance properties, and SINR scaling laws [3][4] While extensive literature has examined large-scale urban macrocell networks under infinite-plane assumptions [5][6], campus-scale deployments remain comparatively underexplored.

In this paper, the base-station deployments at the Federal University of Technology Akure (FUTA) campus are the focus. Visual inspection and coordinate projection of the measured BS locations reveal that the infrastructure does not follow a deterministic hexagonal layout; instead, the spatial arrangement appears irregular and non-uniform. Motivated by this observation, a data-calibrated HPPP baseline derived directly from the measured FUTA coordinates is constructed. The objective is not to claim that the HPPP is the “best” spatial model for FUTA, rather, the goal is to establish a rigorous, reproducible, and analytically grounded first baseline for the campus network. Specifically, this paper (i) estimates the spatial density parameter from the empirical dataset, (ii) compute downlink SINR coverage and outage probability, and (iii) characterize rate probability (rate coverage) under a standard downlink model with Rayleigh fading and nearest-BS association. This baseline provides a consistent reference for future investigations that may

incorporate alternative point processes such as cluster, cox or repulsive models [7][8][9].

To benchmark spatial regularity effects, the same deployment density was also modelled using a deterministic hexagonal grid (Hexgrid) model. The comparative study between the data-calibrated HPPP and the density-matched Hexgrid allows isolation of geometric variability effects on coverage and rate performance, consistent with recent spatial comparison frameworks [10]. Furthermore, both spatial models under three propagation assumptions: (i) an empirical FUTA pathloss model obtained from local measurements [11], (ii) the standardized 3GPP propagation model [11], and (iii) a classical power-law model with exponent $\alpha = 4$ were evaluated. This multi-model propagation analysis enables assessment of sensitivity to environmental calibration and theoretical abstraction [12]. Another distinguishing feature of this work is its explicit treatment of the finite spatial window of the FUTA campus. Unlike conventional HPPP analyses conducted on the infinite plane, our study considers a bounded observation region and implements periodic (wrap-around) boundary conditions to mitigate edge bias. This ensures that the simulated interference field remains statistically consistent with spatial stationarity while respecting the physical limits of the campus layout [13] [14]. Additionally, the model behaviour under both noise-limited (SNR) and interference-limited (SIR) regimes were investigated, thereby separating geometry-driven interference effects from thermal-noise dominance. This regime-aware evaluation clarifies the practical operating conditions under which spatial regularity yields measurable gains [15].

The authors are optimistic that this is the first stochastic-geometry-based modeling of the FUTA campus network. By establishing a data-calibrated HPPP baseline and comparing it to a Hexgrid reference under multiple propagation and regime assumptions, this work lays the methodological foundation for subsequent spatial diagnostics and advanced point-process modeling as the campus infrastructure evolves.

The remainder of this paper is organized as follows. Section II reviews related work on PPP baselines, grid benchmarking, propagation-sensitive SG modeling, and finite-network analysis. Section III presents the finite-window downlink system model. Section IV develops the coverage probability analysis under HPPP and Hexgrid deployments. Section V extends the framework to rate coverage. Section VI presents and discusses numerical results. Section VII concludes the paper.

II. Related Works

Stochastic geometry has become an essential analytical framework for evaluating the performance of cellular networks with spatially random base station (BS) deployments. Early foundational work demonstrated the tractability of homogeneous Poisson point processes (HPPP) in deriving closed-form coverage expressions for infinite networks, emphasizing cellular interference and coverage probability as primary performance metrics [16]. Subsequent research extended these classical models to finite domains, where boundary effects alter interference distributions and hence coverage estimates, making corrections such as wrap-around necessary for realistic comparisons [17], [18].
Recent studies have investigated coverage and rate distributions under increasingly realistic channel assumptions, including multi-antenna transmission, generalized fading, and mmWave propagation, highlighting the sensitivity of SINR metrics to pathloss and blockage effects [19], [20]. Tools such as meta-distributions have been proposed for fine-grained reliability analysis beyond average coverage probability. Distinct from HPPP, alternative point processes including repulsive and clustered models have been employed to capture spatial correlations and regularity in BS deployments, revealing significant impacts on coverage and interference statistics [21], [22].

Multi-tier heterogeneous network (HetNet) analysis using PPPs remains a vibrant area, demonstrating how density, power control, and network architecture influence coverage and spectral efficiency [23], [24]. Works focusing on uplink and downlink coverage probabilities under different PPP assumptions have also characterized the interplay between BS density and SINR performance [25]. Recent surveys have further highlighted the application of stochastic geometry across emerging network paradigms such as integrated sensing and communications (ISAC) and aerial-terrestrial networks [22].

Pathloss modeling itself has attracted extensive study, with empirical and standardized models such as 3GPP pathloss formulations informing coverage predictions across UMi and UMa scenarios [26]. Moreover, rain attenuation and environmental factors have been integrated into pathloss predictions to tailor cellular design to urban morphologies [27].

Despite these advances, few studies conduct controlled benchmarking between HPPP and deterministic Hexgrid deployments under identical density, propagation, regime, and finite-window assumptions. The present work addresses this gap by integrating propagation sensitivity, regime separation, and boundary correction into a unified campus-scale stochastic-geometry framework.

III. FINITE-WINDOW DOWNLINK SYSTEM MODEL

A. Observation Window and Spatial ConfigurationsAbbreviations and Acronyms

Let the campus study region be represented by a finite square observation window given as Equation (1):

$$W = [0, L) \times [0, L), \qquad (1)$$

where L denotes the side length (in meters) and $| W | = L^2$ denotes the window area. All geographical coordinates are projected from WGS84 latitude/longitude into a planar UTM coordinate system to enable Euclidean distance computation in meters. Let $(x_i, y_i) \in W, i = 1, \ldots, N$, where (x_i, y_i) denote the base-station (BS) planar coordinates, and $N = 20$ be the number of active base stations in FUTA campus. Fig. 1 presents the spatial distribution of the 20 active FUTA base stations within the observation window W.

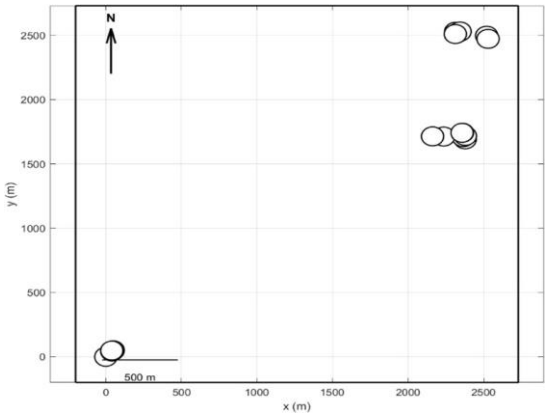

Fig. 1: Projected Planar BS Locations of FUTA BS over the Observation Window W

Two synthetic spatial models were constructed for benchmarking:

1) Homogeneous Poisson Point Process: BSs were modelled as a Poisson point process Φ with calibrated intensity $\hat{\lambda}$ expressed in Equation (2) as:

$$\hat{\lambda} = \frac{N}{| W |}. \qquad (2)$$

Each realization contains a Poisson-distributed number of BSs with mean $\hat{\lambda} | W | = N$.

2) Hexagonal Grid (Hexgrid): A regular hexagonal lattice was generated such that its density matches $\hat{\lambda}$. If D denotes the inter-site distance (ISD), density matching yields Equation (3):

$$\hat{\lambda} = \frac{2}{\sqrt{3}D^2}, \qquad (3)$$

from which D is computed. This density calibration ensures that spatial comparisons isolate regularity versus randomness, rather than density effects.

B. User Distribution and Association Rule

Users are assumed to be independently and uniformly distributed within W. Let

$$\mathrm{u} = (x_u, y_u) \in W \qquad (4)$$

denote the typical user location, where x_u and y_u denote user coordinates. User association follows the maximum-average-received-power rule, which under equal transmit power reduces to nearest-BS association as given in Equation (5):

$$r_0 = \min_{i \in \Phi} \| \mathrm{x}_i - \mathrm{u} \|. \qquad (5)$$

The serving BS index i_0 is therefore expressed as Equation (6):

$$i_0 = \arg\min_{i \in \Phi} r_i. \qquad (6)$$

C. Wrap-Around Distance Model (Edge-Effect Elimination)

Because the analysis was conducted within a finite window, naive Euclidean distance computation would underestimate interference for users near boundaries. To restore statistical homogeneity, periodic boundary conditions were imposed. For each BS x_i, axis-wise displacement relative to user u is computed as Equation (7):

$$\Delta x_i = x_i - x_u, \Delta y_i = y_i - y_u. \qquad (7)$$

The wrapped separations δx_i and δy_i are expressed as Equation (8) and (9):

$$\delta x_i = \min(| \Delta x_i |, L - | \Delta x_i |), \qquad (8)$$
$$\delta y_i = \min(| \Delta y_i |, L - | \Delta y_i |). \qquad (9)$$

The toroidal distance r_i is then computed as Equation (10):

$$r_i = \sqrt{\delta x_i^2 + \delta y_i^2}. \qquad (10)$$

This effectively selects the nearest periodic image of each BS without explicitly replicating the window. All serving and interference distances are computed using (10). Fig. 2 shows the periodic tiling viewpoint (a 3×3 replication of W) and the "nearest-image" distance used in wrap-around computation.

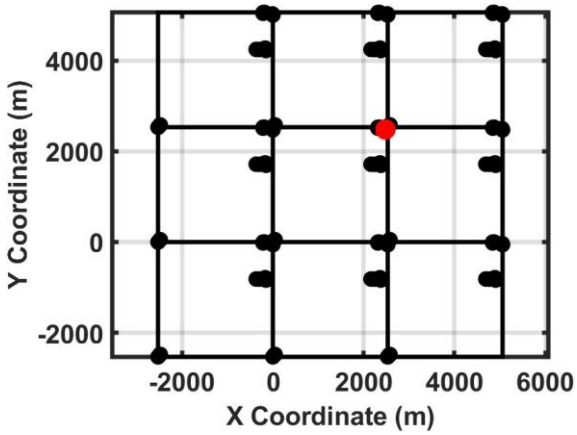

Fig. 2. Wrap-around periodic tiling viewpoint (a 3 × 3 replication of W)

D. Channel Model

Each BS transmits with equal power. Small-scale fading is modelled as independent Rayleigh fading $h_i \sim \exp(1)$, so that channel power gains are exponentially distributed with unit mean. Large-scale pathloss $L(r)$ is represented generically expressed as Equation (11):

$$L(r) = Kr^{-\alpha} \qquad (11)$$

where r signals the distance between the BS and the user, K is the propagation constant and α is the pathloss exponent. Shadowing is omitted to preserve analytical tractability and isolate spatial-structure effects.

E. Signal-to-Interference-and-Noise (SINR) Definition

The downlink SINR at the typical user is given as Equation (12):

$$\mathrm{SINR} = \frac{Ph_0L(r_0)}{\sigma^2 + \sum_{i\in\Phi\setminus i_0} P\, h_iL(r_i)}, \qquad (12)$$

where P is the transmit power, h_0 is the serving-link fading gain, $L(r_0)$ is the serving-link pathloss, h_i is the interfering-link fading, and σ^2 is the noise power which is given as Equation (13):

$$\sigma^2 = kTBF, \qquad (13)$$

where k is Boltzmann's constant, T is temperature (290 K), B is bandwidth, and F is receiver noise figure.

IV. COVERAGE PROBABILITY ANALYSIS

This section develops the coverage probability expressions under the density-matched HPPP baseline and specifies the evaluation procedure for the Hexgrid benchmark under identical physical assumptions. The analysis is carried out in the finite observation window W , while boundary bias is eliminated in simulations using the wrap-around (toroidal) distance definition already introduced in (7) – (10). The derivations below follow the standard stochastic-geometry route for PPP cellular networks under Rayleigh fading [28].

A. Network Geometry and Spatial Models

All base-station geometries were defined within the same finite observation window W and planar coordinate system. To enable density-controlled benchmarking, three spatial configurations were considered. The empirical FUTA deployment was treated as a fixed realization of the 20 measured BS locations, preserving the observed irregular geometry as shown in Fig.3. A homogeneous Poisson point process (HPPP) was adopted as the stochastic baseline, with intensity matched to the empirical density and wrap-around correction applied to mitigate boundary bias shown in Fig. 4. A density-matched Hexgrid was introduced as a regular benchmark to isolate geometric effects as shown in Fig. 5. Together, these models fixed density while varying spatial regularity systematically.

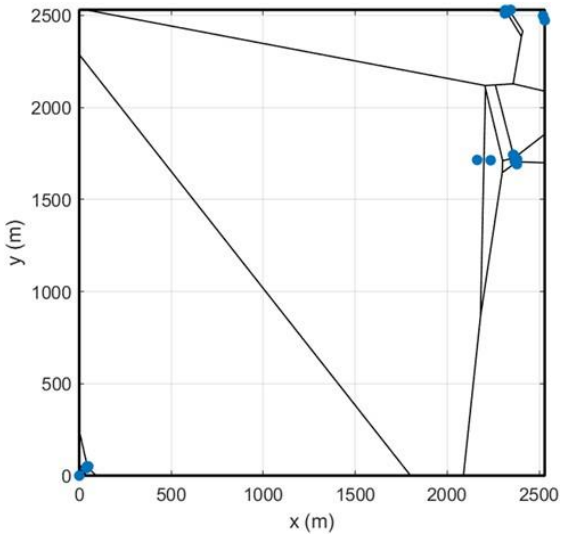

Fig. 3. Voronoi tessellation of the empirical FUTA deployment (nearest-BS service regions)

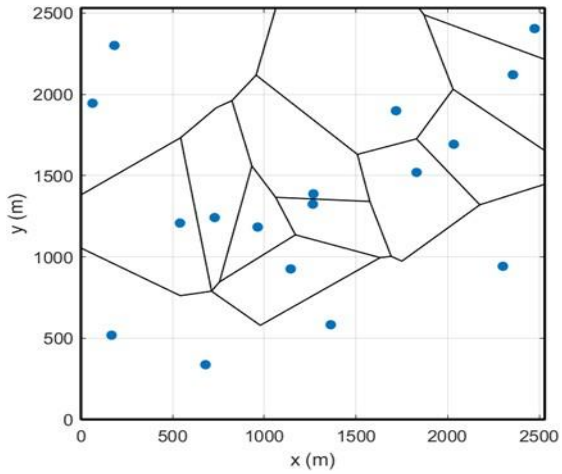

Fig. 4. Voronoi tessellation of a density-matched HPPP realization (one realization).

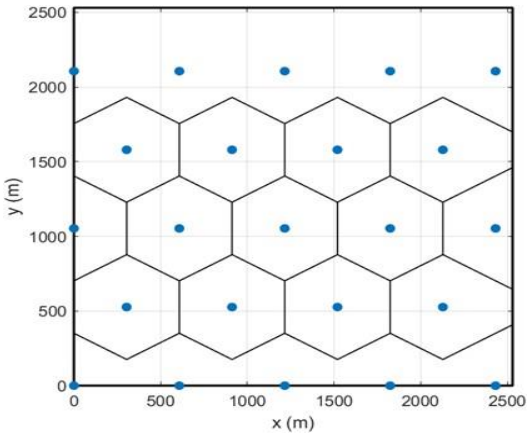

Fig. 5. Voronoi tessellation of the density-matched Hexgrid deployment (regular benchmark).

B. Definition of Coverage Probability

For an SINR threshold $\theta > 0$, coverage probability is defined as given in Equation (14):

$$P_c(\theta) \triangleq \mathbb{P}(\text{SINR} > \theta). \quad (14)$$

Using (12), and denoting the serving distance by $R_0 = r_{i_0}$, the SINR at the typical user is written as:

$$\text{SINR} = \frac{P h_0 L(R_0)}{\sigma^2 + I}, I \triangleq \sum_{i \in \Phi \setminus i_0} P\, h_i L(r_i). \quad (15)$$

Since transmit powers are identical across BSs, the factor P cancels in SINR-based coverage; thus, the coverage probability depends on geometry, propagation, and noise/interference balance, not on the absolute value of P (for fixed σ^2).

C. HPPP Coverage Probability Derivation Under Rayleigh Fading

Under the homogeneous Poisson point process (HPPP) model Φ with spatial intensity λ, the nearest-base-station (serving) distance R_0 follows the well-known distribution derived from the void probability of the PPP expressed in Equation (16):

$$f_{R_0}(r) = 2\pi\lambda r e^{-\pi\lambda r^2}, r \geq 0 \quad (16)$$

with cumulative distribution function $F_{R_0}(r) = 1 - e^{-\pi\lambda r^2}$. This serving-distance law forms the entry point for conditioning in coverage analysis. Conditioning on $R_0 = r$ and assuming Rayleigh fading $h_0 \sim \exp(1)$, the conditional coverage probability is given in Equation (17):

$$\mathbb{P}(\text{SINR} > \theta \mid R_0 = r) = \mathbb{P}\left(h_0 > \frac{\theta(\sigma^2 + I)}{PL(r)}\right) \quad (17)$$

Using the exponential distribution of h_0, this becomes Equation (18):

$$\mathbb{P}(\text{SINR} > \theta \mid R_0 = r) = \exp\left(-\frac{\theta\sigma^2}{PL(r)}\right)\mathcal{L}_I\left(\frac{\theta}{PL(r)}\right) \quad (18)$$

where $\mathcal{L}_I(s) = \mathbb{E}[e^{-sI}]$ denotes the Laplace transform of the aggregate interference.

Under nearest-BS association, interferers lie in $\mathbb{R}^2 \setminus b(0,r)$. Using the probability generating functional (PGFL) of the PPP and i.i.d. Rayleigh fading on interferers [31], the Laplace transform is expressed in Equation (19):

$$\mathcal{L}_I(s \mid R_0 = r) = \exp\left(2\pi\lambda \int_r^\infty \frac{sPL(u)}{1 + sPL(u)} u\, du\right) \quad (19)$$

substituting $s = \frac{\theta}{PL(r)}$ yields Equation (20):

$$\mathcal{L}_I\left(\frac{\theta}{PL(r)} \mid R_0 = r\right) = \exp\left(2\pi\lambda \int_r^\infty \frac{\theta \frac{L(u)}{L(r)}}{1 + \theta\frac{L(u)}{L(r)}} u\, du\right) \quad (20)$$

where the propagation model enters exclusively through the ratio $L(u)/L(r)$.

Deconditioning over R_0 gives the final integral expression for PPP coverage probability expressed in Equation (21):

$$P_c^{\text{PPP}}(\theta) = \int_0^\infty exp\left(-\frac{\theta\sigma^2}{PL(r)}\right)\exp\left(2\pi\lambda \int_r^\infty \frac{\theta\frac{L(u)}{L(r)}}{1 + \theta\frac{L(u)}{L(r)}} u\, du\right) 2\pi\lambda r e^{-\pi\lambda r^2}\, dr \quad (21)$$

For the classical single-slope power-law pathloss $L(r) = r^{-\alpha}$, $\alpha > 2$, the ratio becomes $L(u)/L(r) = (u/r)^{-\alpha}$, leading to the compact form [4] expressed in Equation (22):

$$\mathcal{L}_I(\cdot) = \exp\left(2\pi\lambda r^2 \int_1^\infty \frac{\theta t^{-\alpha}}{1 + \theta t^{-\alpha}} t\, dt\right). \quad (22)$$

Substituting into (21) yields the familiar single-integral representation for PPP coverage under Rayleigh fading and single-slope propagation.

D. Regime-Specific Coverage

To separate operating regimes, two limiting cases are evaluated.

1) *Interference-limited regime (SIR)*: Setting $\sigma^2 \to 0$ in (22) yields Equation (23):

$$P_{c,\text{SIR}}^{\text{PPP}}(\theta) = \int_0^\infty \exp\left(2\pi\lambda \int_r^\infty \frac{\theta\, L(u)/L(r)}{1 + \theta\, L(u)/L(r)} u\, du\right) 2\pi\lambda r e^{-\pi\lambda r^2} \quad (23)$$

For power-law pathloss, the resulting expression becomes density-invariant in the infinite-plane model, a classical result often used to interpret PPP coverage curves under SIR evaluation [28].

2) *Noise-limited regime (SNR):* Suppressing interference ($I = 0$) gives Equation (24):

$$P_{c,\mathrm{SNR}}^{\mathrm{PPP}}(\theta) = \int_0^{\infty} \exp\left(\frac{\theta\sigma^2}{P\,L(r)}\right) 2\pi\lambda r e^{-\pi\lambda r^2}\, dr \qquad (24)$$

This form isolates the dependence on the received-signal distribution and noise floor through $\sigma^2 = kTBF$, providing a clean baseline for understanding bandwidth/noise-figure impacts.

E. Hexagonal Grid Benchmark

Unlike the PPP case, the Hexgrid does not admit a simple nearest-distance distribution in the same closed form under random user locations and finite-window constraints. Consequently, coverage under Hexgrid is evaluated using a semi-analytic Monte Carlo approach that retains identical physical assumptions (transmit power, Rayleigh fading, association rule, and pathloss model) and differs only in the spatial BS geometry. Let Φ_{hex} denote the deterministic lattice realization clipped to the window W and calibrated via (3). For each user drop $\mathrm{u} \sim \mathrm{Unif}(W)$:

- All BS–user distances $\{r_i\}$ are computed using the toroidal metric (10), ensuring consistent edge handling across PPP and Hexgrid.
- The serving BS is selected using nearest-distance association as in (5)–(6) (equivalently maximum average power under equal P).
- Rayleigh fading samples $\{h_i\}$ are generated independent and identically distributed.
- SINR is computed using (12), and the indicator $\mathbb{1}\{\mathrm{SINR} > \theta\}$ is recorded.

The Hexgrid coverage estimate is given as Equation (25):

$$\hat{P}_c^{\mathrm{hex}}(\theta) = \frac{1}{N_{\mathrm{MC}}} \sum_{m=1}^{N_{\mathrm{MC}}} \mathbb{1}\{\mathrm{SINR}_m > \theta\} \qquad (25)$$

where N_{MC} denotes the total number of Monte Carlo trials (across independent user drops and fading realizations).

F. Pathloss Models Considered

1) *Empirical FUTA Log-distance Pathloss Model (Measurement Anchored)*

The empirical propagation model adopted for FUTA was obtained from the measurement-based study of [11] and was adapted here as a single-slope log-distance pathloss law anchored at a reference distance of 400 m. This approach preserves the measured large-scale attenuation trend, while keeping the model compact enough for stochastic-geometry analysis and for fair benchmarking across spatial layouts. Let r(m) denote the link distance between a BS and a user (computed in the planar UTM domain). The empirical pathloss in dB is written as Equation (26):

$$PL_{\mathrm{FUTA}}(r) = PL_{400} + 10n\log_{10}\left(\frac{r}{400}\right), r \geq r_{\min} \qquad (26)$$

Where $PL_{400} = 150$ dB is the measured (or fitted) pathloss at 400 m, $n = 3.5$ is the measured pathloss exponent, and $r_{\min}$ is a small-distance cutoff used to avoid unrealistically small distances in simulation. If $PL(r)$ was first available at two measurement anchors $(d_1, PL(d_1))$ and $(d_2, PL(d_2))$, the exponent n follows directly from the slope of the log-distance law Expressed in Equation (27):

$$n = \frac{PL(d_2) - PL(d_1)}{10\log_{10}\left(\frac{d_2}{d_1}\right)} \qquad (27)$$

This is the exact quantity that controls how fast received power decays with distance, and it is the main reason the empirical model can produce noticeably different coverage/rate curves from standardized models even when $f_c$is identical. Finally, the corresponding large-scale channel gain used inside SINR simulations is expressed as equation (28):

$$L_{\mathrm{FUTA}}(r) = 10^{-\frac{PL_{\mathrm{FUTA}}(r)}{10}} \qquad (28)$$

2) *3GPP Urban Macro (UMa) Model*

For standardized benchmarking, the 3GPP Urban Macrocell (UMa) model was adopted[11]. This model is widely used for sub-6 GHz macro deployments and incorporates distance-dependent LOS/NLOS behavior. In the UMa model, links may be LOS or NLOS, and the pathloss depends on the 3D separation $d_{3\mathrm{D}}$ and a breakpoint distance d_{BP}. The breakpoint is defined as Equation (29):

$$d_{\mathrm{BP}} = \frac{2\pi h_{\mathrm{BS}} h_{\mathrm{UT}} f_c}{c} \qquad (29)$$

where $c = 3 \times 10^8$ m/s is the speed of light, h_{BS} and h_{UT} are BS and UE heights, and f_c is the carrier frequency in Hz. Using the 3GPP UMa outdoor formulation, the LOS pathloss (dB) is given in a two-slope form (before/after the breakpoint) as expressed in Equation (30):

$$PL_{\mathrm{UMa,LOS}}(d_{3\mathrm{D}}) = \begin{cases} 28 + 22\log_{10}(d_{3\mathrm{D}}) + 20\log_{10}(f_c), & 10 \leq d_{2\mathrm{D}} \leq d_{\mathrm{BP}}, \\ 28 + 40\log_{10}(d_{3\mathrm{D}}) + 20\log_{10}(f_c) - 9\log_{10}\left(d_{\mathrm{BP}}^2 + (h_{\mathrm{BS}} - h_{\mathrm{UT}})^2\right), & d_{\mathrm{BP}} < d_{2\mathrm{D}} \leq 5000, \end{cases} \qquad (30)$$

and the NLOS pathloss is applied as given in Equation (31):

$$PL_{\mathrm{UMa,NLOS}}(d_{3D}) = \max\left(PL_{UMa,LOS}(d_{3D}),\, PL'_{UMa,NLOS}(d_{3D})\right) \quad (31)$$

with $PL'_{\mathrm{UMa,NLOS}}$ given by the (scenario-defined) NLOS expression. The LOS probability is distance-dependent. For UMa it follows as given in Equation (32):

$$\Pr_{\mathrm{LOS}}(d_{2D}) = \min\left(\frac{18}{d_{2D}}, 1\right)\left(1-e^{-\frac{d_{2D}}{63}}\right) + e^{-\frac{d_{2D}}{63}} \quad (32)$$

with d_{2D} in meters. Compared to the empirical FUTA model, 3GPP may produce milder attenuation at moderate distances depending on scenario assumptions, thus affecting both serving power and interference aggregation.

3) Classical Power Law Model

To preserve analytical tractability and provide a canonical stochastic-geometry reference, a single-slope power-law model was also considered as given in Equation (33):

$$L_{\mathrm{PL}}(r) = (\max(r, r_{\min}))^{-\alpha}, \alpha = 4. \quad (33)$$

In dB form, (33) is expressed as Equation (34):

$$PL_{\mathrm{PL}}(r) = 10\alpha \log_{10}(\max(r, r_{\min})) + C_0, \quad (34)$$

where C_0 is an intercept chosen for calibration consistency. The exponent $\alpha = 4$ corresponds to a strongly scattering macro environment. Under stochastic geometry, α directly governs the convergence of interference integrals and the tail behaviour of coverage probability.

V. RATE-COVERAGE PROBABILITY ANALYSIS

This section develops the rate (or spectral-efficiency) coverage under the same spatial models, propagation assumptions, and regime definitions used for coverage probability in Section IV.

A. Rate-Coverage Definitions

Let B denote the system bandwidth (Hz), the instantaneous downlink rate (bps) experienced by the typical user is modelled using the Shannon form expressed in Equation (35):

$$R = B\log_2(1 + \mathrm{SINR}), \quad (35)$$

and the spectral efficiency (bps/Hz) is expressed in Equation (36):

$$\eta = \log_2(1 + \mathrm{SINR}). \quad (36)$$

Two equivalent forms of rate coverage were used.

1) Rate coverage at absolute-rate threshold ρ(bps): This is expressed as Equation (37):

$$P_r(\rho) \triangleq \mathbb{P}(R > \rho) = \mathbb{P}(B\log_2(1 + \mathrm{SINR}) > \rho) \quad (37)$$

2) Spectral-efficiency coverage at threshold τ(bps/Hz): This is expressed as Equation (38):

$$P_\eta(\tau) \triangleq \mathbb{P}(\eta > \tau) = \mathbb{P}(\log_2(1 + \mathrm{SINR}) > \tau) \quad (38)$$

The spectral-efficiency form is convenient because it is independent of bandwidth scaling.

B. SINR Threshold Mapping

By re-arranging (39), Equation (39) is obtained as:

$$\log_2(1 + \mathrm{SINR}) > \tau \Leftrightarrow \mathrm{SINR} > 2^\tau - 1. \quad (39)$$

By defining the SINR-equivalent threshold as $\theta(\tau) \triangleq 2^\tau - 1$, the rate coverage is directly obtained from the coverage probability evaluated at $\theta(\tau)$ as expressed in Equation (40):

$$P_\eta(\tau) = P_c(\theta(\tau)) = P_c(2^\tau - 1). \quad (40)$$

Similarly, for absolute-rate threshold ρ, the equivalent spectral-efficiency threshold is $\tau(\rho) = \rho/B$, yielding Equation (41):

$$P_r(\rho) = \mathbb{P}\left(\mathrm{SINR} > 2^{\frac{\rho}{B}} - 1\right) = P_c\left(2^{\frac{\rho}{B}} - 1\right) \quad (41)$$

Equations (40)–(41) ensure that once $P_c(\theta)$ is available analytically for PPP or numerically for Hexgrid, rate coverage follows without re-deriving a second interference expression.

C. HPPP Baseline: Rate-Coverage in the Full SINR Model

Using the PPP coverage integral in (21), the spectral-efficiency coverage is obtained as Equation (42):

$$P_\eta^{\mathrm{PPP}}(\tau) = P_c^{\mathrm{PPP}}(2^\tau - 1), \quad (42)$$

Equation (21) is evaluated at $\theta = 2^\tau - 1$. Writing it explicitly for clarity, Equation (43) is obtained as:

$$P_\eta^{\mathrm{PPP}}(\tau) = \int_0^\infty exp\left(\frac{(2^\tau - 1)\sigma^2}{P\,L(r)}\right) exp\left(2\pi\lambda \int_r^\infty \frac{(2^\tau - 1)\,L(u)/L(r)}{1 + (2^\tau - 1)\,L(u)/L(r)} u\,du\right) 2\pi\lambda r e^{-\pi\lambda r^2}\,dr \quad (43)$$

Equation (43) highlights that propagation-model sensitivity enters rate coverage through the same pathloss ratio $L(u)/L(r)$ and noise scaling $1/L(r)$ that govern coverage probability.

D. Regime-Specific Rate Coverage (SIR and SNR)

The regime separation from Section IV carries over directly under the threshold mapping.

1) *Interference-limited regime (SIR-rate):* Replacing $P_c^{\mathrm{PPP}}(\theta)$ by its SIR form in (23) yields Equation (44):

$$P_{\eta,\mathrm{SIR}}^{\mathrm{PPP}}(\tau) = P_{c,\mathrm{SIR}}^{\mathrm{PPP}}\,(2^{\tau}-1). \qquad (44)$$

This regime emphasizes spatial geometry and pathloss shaping of interference, with no explicit dependence on B or F because σ^2 is suppressed.

2) *Noise-limited regime (SNR-rate):* Suppressing interference and using (24) yields Equation (45):

$$P_{\eta,\mathrm{SNR}}^{\mathrm{PPP}}(\tau) = P_{c,\mathrm{SNR}}^{\mathrm{PPP}}\,(2^{\tau}-1). \qquad (45)$$

This regime makes the dependence on $\sigma^2 = kTBF$ explicit through $\theta(\tau)\sigma^2$, so bandwidth and noise figure directly shift the rate coverage curve.

E. Hexgrid Benchmark: Rate-Coverage Estimation

For the Hexgrid deployment, rate coverage is evaluated by Monte Carlo under the same assumptions as the PPP simulations (Rayleigh fading, identical transmit power, same association rule
The spectral-efficiency coverage estimate is given as expressed in Equation (46):

$$\hat{P}_{\eta}^{\mathrm{hex}}(\tau) = \frac{1}{N_{\mathrm{MC}}}\sum_{m=1}^{N_{\mathrm{MC}}} \mathbb{1}\{\eta_m > \tau\}, \qquad (46)$$

and the absolute-rate coverage estimate is given as Equation (47):

$$\hat{P}_{r}^{\mathrm{hex}}(\rho) = \frac{1}{N_{\mathrm{MC}}}\sum_{m=1}^{N_{\mathrm{MC}}} \mathbb{1}\{R_m > \rho\}. \qquad (47)$$

As with coverage probability, wrap-around distances are applied universally in all Hexgrid simulations to remove boundary bias and ensure consistency with PPP simulations.

VI. RESULTS AND DISCUSSION

This section presents the performance evaluation of the density-matched HPPP and Hexgrid spatial models under the three propagation models (empirical FUTA, 3GPP UMa, and power-law $\alpha = 4$). Results are organized into coverage probability, rate probability, and spatial diagnostics. All simulations employ the toroidal wrap-around distance model introduced earlier to eliminate boundary bias in the finite observation window.

All coverage and rate results presented in this section are obtained under a unified set of spatial, propagation, and system parameters summarized in Table I. The table consolidates the density calibration of the HPPP and Hexgrid models, transmit and channel assumptions, propagation model specifications, regime definitions, and simulation settings to ensure reproducibility and consistent cross-comparison across figures. Unless otherwise stated, every result discussed in this section follows the configuration listed in Table I.

Table I: System and Simulation Parameters Used in This Study

Category	Parameter	Symbol	Value	Notes
Spatial Model	Number of BS (empirical)	N	20	Measured FUTA dataset
	Observation window area	W	6400 m^2	Measured FUTA area
	Window side length	L	2529.82 m	Square region
Transmit Parameters	Transmit power	P_t	20 W	Same for all BS
	Carrier frequency	f_c	2.6 GHz	Used in 3GPP
	Bandwidth	B	20 MHz	Downlink
	Noise figure	F	7 dB	Receiver
	Temperature	T	290 K	Thermal noise
Fading Model	Small-scale fading	h	Exp(1)	Rayleigh
Empirical FUTA Pathloss	Reference pathloss at 400 m	PL_{400}	150 dB	Measured
	Pathloss exponent	n	3.5	Measured
	Reference distance	d_0	400 m	Anchor
3GPP Model (UMa)	BS height	h_{BS}	30 m	Assumed
	UE height	h_{UT}	1.5 m	Standard
	Scenario	—	UMa	Urban macro
	LOS probability	—	Distance-dependent	3GPP TR 38.901
Power-Law Model	Pathloss exponent	α	4	Classical SG reference
	Spectral efficiency	τ	bps/Hz	$\log_2(1 + \mathrm{SINR})$

A. Network Geometry and Spatial Models

1) Coverage Probability under Full SINR

Fig. 6 presents the downlink coverage probability $P_c(\theta)$ for the FUTA deployment under full SINR operation. Three pathloss propagation models are evaluated under both HPPP and Hexgrid spatial assumptions over the threshold range -10 to 30 dB.

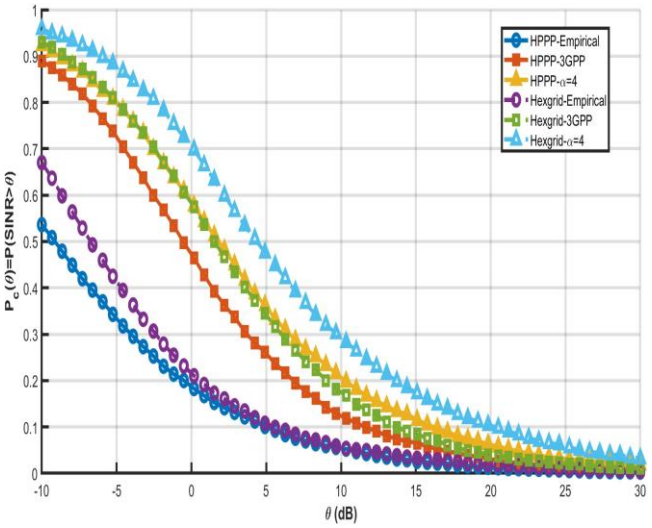

Fig. 6. Downlink coverage probability under full SINR operation for HPPP and Hexgrid deployments using empirical FUTA, 3GPP (UMa), and power-law ($\alpha = 4$) pathloss propagation models

Across all propagation models, Hexgrid achieves higher coverage probability than HPPP at moderate thresholds. For example, at $\theta = 0$ dB, Hexgrid improves coverage by approximately 12 percentage points under the 3GPP model and 11 percentage points under the $\alpha = 4$ model, while the empirical FUTA model shows a smaller 3-point improvement. These gains result from reduced interference variability and narrower serving-distance dispersion under deterministic geometry.

However, the spatial advantage diminishes as the SINR threshold increases. At $\theta = 20$ dB, the improvement drops to approximately 1–2 percentage points across standardized models and becomes negligible under the empirical FUTA model. This indicates that high-SINR reliability is dominated by propagation attenuation rather than purely geometric regularity.

Table II quantifies the spatial coverage gain $\Delta P_c(\theta)$ at representative thresholds. The largest improvements occur at moderate thresholds (0 dB), while gains contract significantly at high thresholds (20 dB). Importantly, the empirical FUTA pathloss model consistently produces smaller spatial gains than the standardized 3GPP and power-law models. This demonstrates that campus-calibrated attenuation reduces the structural advantage of idealized regular deployment.

Table II: Coverage Probability Comparison between HPPP and Hexgrid under Full SINR

Pathloss Model	θ (dB)	HPPP	Hexgrid	ΔPc(θ)
Empirical FUTA	0	0.18	0.21	+0.03
	10	0.05	0.06	+0.01
	20	0.01	0.01	+0.00
3GPP (UMa)	0	0.46	0.58	+0.12
	10	0.13	0.18	+0.05
	20	0.04	0.05	+0.01
Power-Law (α = 4)	0	0.59	0.70	+0.11
	10	0.24	0.29	+0.05
	20	0.07	0.09	+0.02

Although Hexgrid exhibits superior coverage performance, it does not represent the observed spatial configuration of FUTA base stations. The measured deployment reveals irregular spacing and non-uniform angular dispersion driven by physical infrastructure constraints, terrain variations, and practical operator placement decisions. The stochastic variability inherent in HPPP more closely matches this observed geometry. Therefore, Hexgrid should be interpreted as a structured upper-bound benchmark isolating geometric regularity, whereas HPPP constitutes the statistically consistent baseline for modeling FUTA. The coverage analysis confirms that spatial regularity improves SINR reliability, but realistic campus deployment behavior aligns more closely with stochastic spatial modeling than deterministic lattice assumptions.

2) Coverage Regime Separation: Noise and Interference Regime Analysis

Fig. 7 and Fig. 8 isolates noise-limited and interference-limited behavior by separately evaluating SNR-based and SIR-based coverage probabilities. This separation allows diagnosis of whether the observed coverage trends in Fig. 6 are noise-driven or interference-driven.

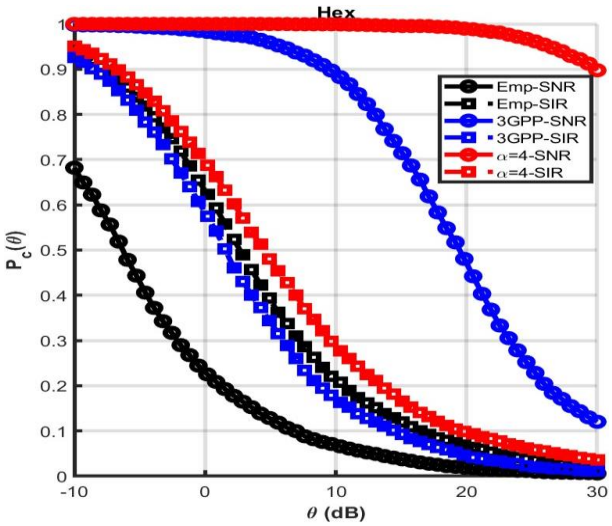

Fig. 7. Coverage probability regime separation under SNR (noise-limited) and SIR (interference-limited) for Hexgrid deployments

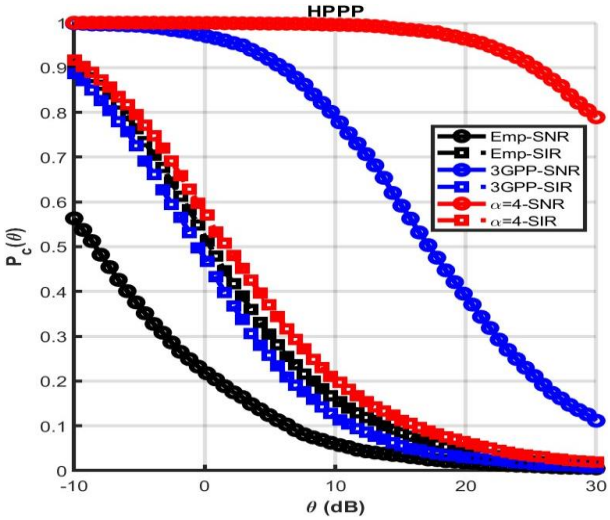

Fig.8. Coverage probability regime separation under SNR (noise-limited) and SIR (interference-limited) for HPPP deployments

Under the 3GPP and $\alpha = 4$ propagation models, SNR curves remain near unity across a wide SINR threshold range, while SIR curves decay rapidly with increasing θ. At $\theta = 0$dB under HPPP, the SNR–SIR separation reaches approximately 0.64 for 3GPP and 0.60 for $\alpha = 4$. At $\theta = 10$dB, the separation increases further to approximately 0.64–0.85. These large gaps confirm that coverage performance under standardized propagation models is predominantly interference-limited.

In contrast, the empirical FUTA pathloss model exhibits minimal SNR–SIR separation. At $\theta = 0$dB, the gap is approximately 0.02 under both spatial deployments, and reduces to approximately 0.01 at $\theta = 10$ dB. This indicates that campus-calibrated attenuation introduces meaningful noise influence, resulting in mixed regime behavior rather than purely interference-limited operation.

Comparing spatial models, Hexgrid slightly reduces SIR degradation relative to HPPP due to lower interference variability. However, regime classification remains unchanged. Under standardized propagation assumptions, the network remains interference-dominated; under empirical attenuation, it exhibits partial noise sensitivity.

These findings demonstrate that regime classification depends strongly on propagation modeling. Standardized 3GPP and power-law models may overstate interference dominance in campus-scale environments, whereas empirical calibration reveals a more nuanced mixed regime. Importantly, although Hexgrid improves raw coverage through geometric regularity, the irregular measured deployment of FUTA base stations aligns more closely with the stochastic variability captured by HPPP. Therefore, HPPP remains the realistic modeling baseline despite its slightly lower interference robustness.

B. Rate-Coverage Probability Results

The rate probability (RP) $P_r(\rho) = \mathbb{P}(R > \rho)$ is evaluated for both HPPP and Hexgrid spatial models under the empirical FUTA, 3GPP, and $\alpha = 4$ pathloss propagation models. Two operating regimes are considered: the full SINR regime and the separated SNR/SIR regimes.

1) Absolute Rate Coverage under full SINR

Fig. 9 and Table III jointly quantify the absolute rate coverage $P_r(\rho)$ under full SINR for density-matched HPPP and Hexgrid deployments across the three propagation models

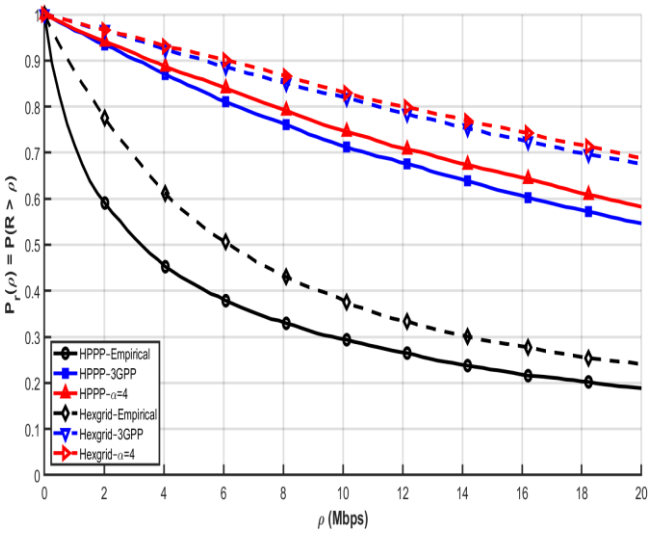

Fig. 9. Absolute rate coverage probability $P_r(\rho) = P(R > \rho)$ under full SINR for density-matched HPPP and Hexgrid deployments in the finite FUTA observation window

Table III: Absolute rate coverage comparison between HPPP and Hexgrid deployments under full SINR operation for three propagation models

Pathloss Model	ρ (Mbps)	HPPP	Hexgrid	ΔPr(ρ)
Empirical FUTA	5	0.38	0.52	+0.14
	10	0.29	0.39	+0.10
	15	0.23	0.31	+0.08
	20	0.19	0.24	+0.05
3GPP (UMa)	5	0.82	0.89	+0.07
	10	0.72	0.83	+0.11
	15	0.62	0.76	+0.14
	20	0.55	0.68	+0.13
Power-Law (α = 4)	5	0.85	0.91	+0.06
	10	0.74	0.84	+0.10
	15	0.66	0.78	+0.12
	20	0.58	0.70	+0.12

Fig. 9 and Table III jointly quantify the absolute rate coverage $P_r(\rho)$ under full SINR for density-matched HPPP and Hexgrid deployments across the three propagation models. As expected, the Hexgrid

configuration consistently achieves higher rate coverage than the HPPP baseline across the entire threshold range. For example, under the 3GPP model at $\rho = 10$ Mbps, Hexgrid attains approximately 0.83 compared to 0.72 for HPPP, yielding a spatial gain of about 11 percentage points. Under the power-law model ($\alpha = 4$), the corresponding improvement is approximately 10 percentage points, while under the empirical FUTA model, the gain is about 10 percentage points at the same threshold. At higher rate targets ($\rho = 15$–20 Mbps), the gain increases under 3GPP and $\alpha = 4$ (reaching 12–14 percentage points), whereas it decreases slightly under the empirical model (down to approximately 5 percentage points at 20 Mbps).

These differences are consistent with the structural properties of the two spatial models. The Hexgrid deployment exhibits reduced serving-distance variance and lower interference dispersion due to its regular geometry, resulting in smoother SINR statistics and improved tail reliability. In contrast, the HPPP model introduces spatial randomness, which increases both serving-distance variability and interference fluctuation, thereby reducing high-rate reliability. The magnitude and threshold-dependence of $\Delta P_r(\rho)$ further indicate that spatial regularity becomes increasingly beneficial as rate requirements become more stringent, particularly under standardized propagation assumptions.

However, while Hexgrid demonstrates superior performance, it does not reflect the actual spatial configuration of base stations on the FUTA campus. The measured BS coordinates exhibit irregular placement driven by terrain constraints, building layouts, infrastructure availability, and operator deployment decisions, rather than the deterministic symmetry assumed by a lattice model. The HPPP, though an abstraction, more closely captures this observed randomness in inter-site distances and angular dispersion. Consequently, the HPPP baseline provides a statistically consistent and structurally representative model for FUTA, even if it yields slightly lower rate coverage compared to the idealized Hexgrid

2) Regime Separation Analysis: Noise-Limited vs Interference-Limited Behavior

Fig. 10 and 11 isolates regime effects by separating SNR (noise-limited) and SIR (interference-limited) behaviour for Hexgrid and HPPP spatial models respectively.

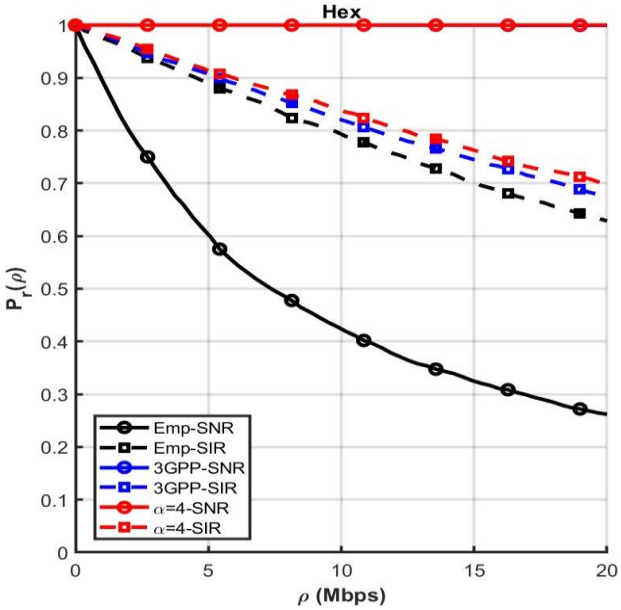

Fig. 10. Regime separation of absolute rate coverage under SNR (noise-limited) and SIR (interference-limited) assumptions for Hexgrid deployments

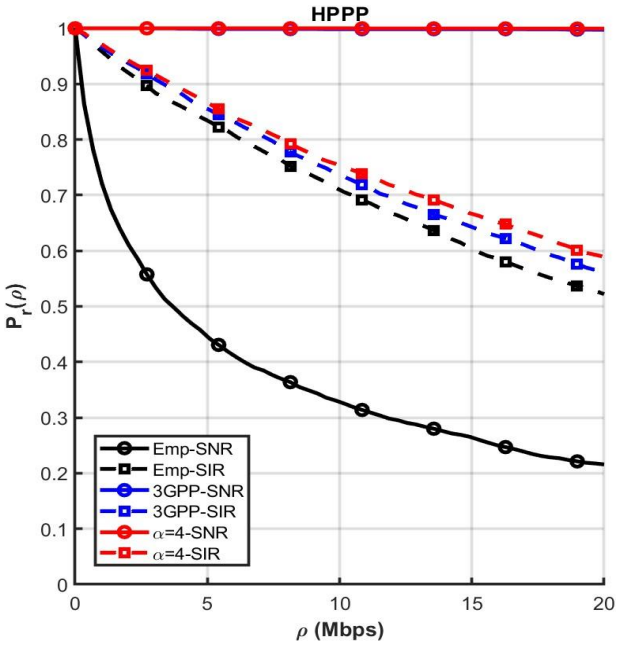

Fig. 11. Regime separation of absolute rate coverage under SNR (noise-limited) and SIR (interference-limited) assumptions for HPPP

Under the standardized 3GPP and power-law ($\alpha = 4$) models, SNR curves remain near unity across the entire 0–20 Mbps range, whereas SIR curves decay steadily with increasing rate threshold. This indicates that the network operates predominantly in an interference-limited regime under these propagation assumptions. In contrast, under the empirical FUTA pathloss model, the SNR curves exhibit noticeable decay and lie closer to the SIR curves, revealing partial noise influence. At 10 Mbps under HPPP, the empirical SNR coverage is approximately 0.31 while the SIR coverage is

approximately 0.29, demonstrating a small regime gap relative to standardized models. Spatial regularity in the Hexgrid deployment slightly reduces SIR degradation due to lower interference variability; however, the regime ordering remains unchanged. These results show that propagation modeling significantly influences regime classification and that campus-calibrated attenuation introduces mixed noise–interference behavior not captured by standardized models alone.

3) Spectral Efficiency Coverage: SINR-Driven Performance

Fig. 12 presents the spectral-efficiency coverage probability over the realistic threshold range $\tau \in [0,5]$ bps/Hz.

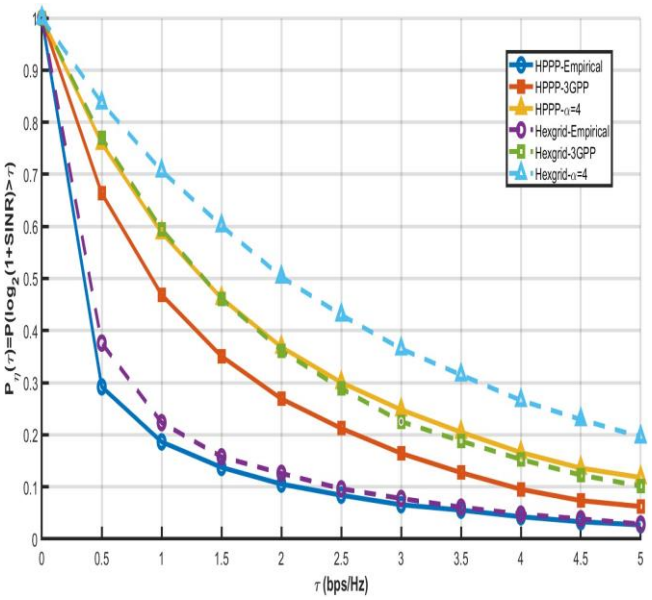

Fig. 12. Spectral-efficiency coverage probability under HPPP and Hexgrid deployments for empirical FUTA, 3GPP (UMa), and power-law ($\alpha = 4$) propagation models

Unlike absolute rate coverage, this metric removes the bandwidth scaling factor and therefore reflects the intrinsic SINR distribution of the network. As a result, any performance differences observed in this figure arise purely from spatial geometry and propagation characteristics rather than bandwidth normalization effects.

Across all propagation models, Hexgrid consistently achieves higher spectral-efficiency coverage than HPPP. For example, at $\tau = 2$ bps/Hz under the 3GPP model, Hexgrid yields approximately 0.36 compared to 0.27 under HPPP, corresponding to a spatial gain of approximately 9 percentage points. Under the $\alpha = 4$ model, the gain at the same threshold is approximately 14 percentage points (0.51 vs 0.37). Even under the empirical FUTA model, where overall coverage is lower, Hexgrid maintains a modest advantage (≈0.13 vs 0.10 at $\tau = 2$).

However, while Hexgrid provides superior spectral efficiency, it does not represent the observed spatial structure of the FUTA deployment. The measured base-station coordinates exhibit irregular spacing and non-uniform angular separation driven by terrain constraints, building density, and infrastructure availability. The deployment does not exhibit lattice symmetry or deterministic inter-site spacing. Consequently, the interference variability and serving-distance randomness inherent in HPPP more closely resemble the empirical geometry. Therefore, although Hexgrid represents a structured upper-performance benchmark, HPPP remains the statistically consistent modeling baseline for FUTA. The spectral-efficiency results confirm that the observed differences are largely driven by SINR distribution effects rather than bandwidth artifacts, and that realistic campus geometry aligns more closely with stochastic spatial modeling than deterministic lattice assumptions.

VII. CONCLUSION

This study developed a finite-window stochastic-geometry framework for modelling campus cellular deployments and evaluating downlink coverage and rate performance within a bounded observation region. Using the measured base-station coordinates of the Federal University of Technology Akure (FUTA), a data-calibrated homogeneous Poisson point process baseline was constructed and benchmarked against a density-matched regular deployment to isolate geometric regularity effects. Periodic wrap-around distance modeling was implemented to eliminate boundary bias and restore statistical homogeneity within the finite spatial window.

Coverage and rate analyses were conducted under three propagation assumptions: an empirical FUTA measurement-based model, the standardized 3GPP Urban Macro formulation, and a classical single-slope power-law model with exponent four. Results demonstrated that spatial regularity improves moderate-threshold reliability, with coverage gains reaching approximately 12% at 0 dB under standardized propagation, while diminishing to nearly negligible levels at high thresholds. Absolute rate coverage at 10 Mbps improved by roughly 10–11% under structured geometry, with gains contracting under empirical campus-calibrated attenuation. Regime separation further revealed predominantly interference-limited behavior under standardized propagation and mixed noise–interference characteristics under empirical calibration. Although the regular benchmark achieved consistently higher performance, the measured FUTA deployment exhibits irregular spacing and non-uniform angular dispersion inconsistent with lattice symmetry. Consequently, the stochastic baseline more closely represents the observed campus geometry while preserving analytical tractability.

The proposed framework establishes the first finite-window stochastic-geometry baseline for FUTA and provides a reproducible foundation for future investigations incorporating advanced spatial point processes, refined propagation models, and infrastructure evolution analysis in campus-scale cellular networks.

REFERENCES

[1] J. G. Andrews, F. Baccelli, and R. K. Ganti, "'A tractable approach to coverage and rate in cellular networks,'" *IEEE Transactions on Communications*, vol. 59, no. 11, pp. 3122–3134, Nov. 2011, doi: 10.1109/tcomm.2011.100411.100541.

[2] B. Błaszczyszyn, M. Haenggi, P. Keeler, and S. Mukherjee, *Stochastic geometry analysis of cellular networks*. Cambridge: Cambridge University Press, 2018. doi: 10.1017/9781316677339.

[3] M. Di Renzo and P. Guan, "Stochastic geometry modeling of coverage and rate of cellular networks using the gil-pelaez inversion theorem," *IEEE Communications Letters*, vol. 18, no. 9, pp. 1575–1578, Sep. 2014, doi: 10.1109/LCOMM.2014.2341251.

[4] H. ElSawy, A. Sultan-Salem, M. S. Alouini, and M. Z. Win, "Modeling and Analysis of Cellular Networks Using Stochastic Geometry: A Tutorial," *IEEE Communications Surveys and Tutorials*, vol. 19, no. 1, pp. 167–203, Jan. 2017, doi: 10.1109/COMST.2016.2624939.

[5] M. A. Ouamri, "Stochastic geometry modeling and analysis of downlink coverage and rate in small cell network," *Telecommunication Systems 2021 77:4*, vol. 77, no. 4, pp. 767–779, Mar. 2021, doi: 10.1007/s11235-021-00770-5.

[6] A. Y. Etcibaşi and E. Aktaş, "Coverage Analysis of IRS-Aided Millimeter-Wave Networks: A Practical Approach," *IEEE Trans. Wirel. Commun.*, vol. 23, no. 4, pp. 3721–3734, Apr. 2024, doi: 10.1109/TWC.2023.

[7] S. M. Azimi-Abarghouyi and H. S. Dhillon, "Matern Cluster Process with Holes at the Cluster Centers," *Stat. Probab. Lett.*, vol. 204, Oct. 2022, doi: https://doi.org/10.1016/j.spl.2023.109931.

[8] N. D'Angelo, M. Siino, A. D'Alessandro, and G. Adelfio, "Local spatial log-Gaussian Cox processes for seismic data," *AStA Advances in Statistical Analysis*, vol. 106, no. 4, pp. 633–671, Dec. 2022, doi: 10.1007/s10182-022-00444-w.

[9] C. Chen, "Modelling and analysis of repulsive cellular networks using Matérn hard-core point processes," *Electron. Lett.*, vol. 60, no. 22, Nov. 2024, doi: 10.1049/ell2.70085.

[10] H. Zhang, L. Feng, T. Zheng, and D. K. Sung, "Characterization of base station deployment distribution and coverage in heterogeneous networks," *IET Communications*, vol. 15, no. 6, pp. 850–865, Apr. 2021, doi: 10.1049/cmu2.12126.

[11] S. O. Oluwatoki, S. A. Busari, and J. J. Popoola, "Empirical Path Loss Modelling for Selected LTE Networks in FUTA Campus, Ondo State, Nigeria," *Journal of Engineering Advancements*, pp. 1–7, Jan. 2023, doi: 10.38032/jea.2023.01.001.

[12] A. Akinbolati and B. T. Abe, "Investigating the Reliability of Empirical Path Loss Models over Digital Terrestrial UHF Channels in Ikorodu and Akure, Southwestern Nigeria," *Telecom*, vol. 6, no. 2, Jun. 2025, doi: 10.3390/telecom6020028.

[13] M. K. M. and M. R. A. Fastenbauer, "Investigation of Wraparound Techniques for the Simulation of Wireless Cellular Networks," in *23rd International ITG Workshop on Smart Antennas*, Vienna, Austria: WSA , 2019, pp. 1–6.

[14] MathsWorks, "NR Interference Modeling with Toroidal Wrap-Around - MATLAB & Simulink." Accessed: Feb. 22, 2026. [Online]. Available: https://www.mathworks.com/help/5g/ug/nr-interference-modeling-with-toroidal-wrap-around.html?utm_source=chatgpt.com

[15] B. Yang, G. Mao, M. Ding, X. Ge, and X. Tao, "Dense small cell networks: From noise-limited to dense interference-limited," *IEEE Trans. Veh. Technol.*, vol. 67, no. 5, pp. 4262–4277, May 2018, doi: 10.1109/TVT.2018.2794452.

[16] Martin. Haenggi, *Stochastic geometry for wireless networks*, vol. 1. Cambridge University Press, 2013.

[17] S. M. Azimi-Abarghouyi, B. Makki, M. Haenggi, M. Nasiri-Kenari, and T. Svensson, "Coverage analysis of finite cellular networks: A stochastic geometry approach," *IWCIT 2018 - Iran Workshop on Communication and Information Theory*, pp. 1–5, Jul. 2018, doi: 10.1109/IWCIT.2018.8405041.

[18] S. M. Azimi-Abarghouyi, B. Makki, M. Nasiri-Kenari, and T. Svensson, "Stochastic geometry modeling and analysis of finite millimeter wave wireless networks," *IEEE Trans. Veh. Technol.*, vol. 68, no. 2, pp. 1378–1393, Feb. 2019, doi: 10.1109/TVT.2018.2883891.

[19] M. Rebato, J. Park, P. Popovski, E. De Carvalho, and M. Zorzi, "Stochastic Geometric Coverage Analysis in mmWave Cellular Networks With Realistic Channel and Antenna Radiation Models," *IEEE Transactions on Communications*, vol. 67, no. 5, pp. 3736–3752, May 2019, doi: 10.1109/TCOMM.2019.2895850.

[20] F. Xu, Y. Hu, Z. Hu, and H. Cao, "Coverage Probability Analysis for Device-to-Device Communication Underlaying Cellular Networks," *Electronics 2022, Vol. 11,* vol. 11, no. 3, Feb. 2022, doi: 10.3390/electronics11030464.

[21] C. Wang, C. Yang, L. Liu, P. Wang, and H. Liu, "Stochastic geometry interference model

for 5G heterogeneous network," *Parallel and Distributed Computing, Applications and Technologies, PDCAT Proceedings*, vol. 0, pp. 286–289, Jul. 2016, doi: 10.1109/PDCAT.2016.067.

[22] H. K. Armeniakos, P. S. Bithas, S. A. Tegos, A. G. Kanatas, and G. K. Karagiannidis, "Stochastic Geometry for Modeling and Analysis of Sensing and Communications: A Survey," *IEEE Communications Surveys and Tutorials*, vol. 28, pp. 2691–2724, 2026, doi: 10.1109/COMST.2025.3594560.

[23] M. M. Fadoul, "Rate and coverage analysis in multi-tier heterogeneous network using stochastic geometry approach," *Ad Hoc Networks*, vol. 98, p. 102038, Mar. 2020, doi: 10.1016/j.adhoc.2019.102038.

[24] Q. Liu and Z. Zhang, "The analysis of coverage probability, ASE and EE in heterogeneous ultra-dense networks with power control," *Digital Communications and Networks*, vol. 6, no. 4, pp. 524–533, Nov. 2020, doi: 10.1016/j.dcan.2020.02.002.

[25] H. Mariam, I. Ahmed, and M. I. Aslam, "Coverage probability of uplink millimeter wave cellular network with non-homogeneous interferers' point process," *Physical Communication*, vol. 45, p. 101274, Apr. 2021, doi: 10.1016/j.phycom.2021.101274.

[26] S. B. Matondo and P. A. Owolawi, "Impact of Rain Attenuation on Path Loss and Link Budget in 5G mmWave Wireless Propagation Under South Africa's Subtropical Climate," *Telecom 2025, Vol. 6,* vol. 6, no. 3, Sep. 2025, doi: 10.3390/telecom6030066.

[27] T. T. Oladimeji, P. Kumar, and N. O. Oyie, "Propagation path loss prediction modelling in enclosed environments for 5G networks: A review," *Heliyon*, vol. 8, no. 11, p. e11581, Nov. 2022, doi: 10.1016/j.heliyon.2022.e11581.

[28] J. G. Andrews, F. Baccelli, and R. K. Ganti, "A tractable approach to coverage and rate in cellular networks," *IEEE Transactions on Communications*, vol. 59, no. 11, pp. 3122–3134, Nov. 2011, doi: 10.1109/TCOMM.2011.100411.100541.